Research Article

Xuemei Yang*, Jinhui Zhao, Xuewei Yan, Xiaonan Shi, and Hongzhen Guo

The dynamic softening identification and constitutive equation establishment of Ti-6.5Al-2Sn-4Zr-4Mo-1W-0.2Si alloy with initial lamellar microstructure

https://doi.org/10.1515/htmp-2022-0242 received June 12, 2022; accepted September 12, 2022

Abstract: The high-temperature deformation behavior of Ti-6.5Al-2Sn-4Zr-4Mo-1W-0.2Si alloy with initial lamellar microstructure was investigated through performing hot compression experiments at temperatures of 940-1,030°C and strain rates of 0.001-10 s⁻¹ on the Gleeble-3500 simulator. Three kinds of typical flow curves corresponding to different strain rates were distinguished. The deformation activation energy and Zener-Hollomon parameter were obtained through kinetic analysis. By comparing saturated dislocation density with the critical density for dynamic recrystallization, dynamic softening behaviors were identified and verified by the Poliak-Jonas criterion. Furthermore, a piecewise physical-based constitutive model incorporating dynamic softening behaviors was constructed. Finally, microstructures deformed under different deformation conditions were analyzed to further verify the softening behaviors determined by identification criterions.

Keywords: titanium alloy, dynamic softening, dislocation evolution, constitutive model

Jinhui Zhao: School of Aerospace Engineering, Zhengzhou University of Aeronautics, Zhengzhou 450046, PR China Xuewei Yan: School of Aero Engine, Zhengzhou University of

Aeronautics, Zhengzhou 450046, PR China

Xiaonan Shi: School of Civil Aviation, Zhengzhou University of

Aeronautics, Zhengzhou 450046, PR China

Hongzhen Guo: School of Materials Science and Engineering, Northwestern Polytechnical University, Xi'an 710072, PR China

1 Introduction

The Ti-6.5Al-2Sn-4Zr-4Mo-1W-0.2Si alloy owns prominent comprehensive mechanical performance at high service temperatures [1]. For the past few years, owing to the potential for manufacturing dual-property compressor blisk, Ti-6.5Al-2Sn-4Zr-4Mo-1W-0.2Si alloy has gained considerable concern. The dual-property blisk is designed to be composed of equiaxed microstructure at the disc core and basketweave microstructure at the blade section in view of the different working environments and performance requirements between two compressor parts [2]. Generally, the mechanical properties of titanium alloys largely depend on the deformation parameters and corresponding microstructures. Constitutive relationship is often used to reflect the mechanical response to deformation parameters, and dynamic softening behaviors determine the evolution of microstructure during high-temperature deformation. Thus, in order to optimize the deformation parameters and obtain favorable microstructure, it is very important to identify the dynamic softening behaviors and establish the constitutive relationship model.

The dynamic softening behavior and constitutive relationship of titanium alloys during hot deformation have been studied extensively. Zyguła et al. [3] calculated the deformation activation energy and Zener–Hollomon parameter of powder metallurgy Ti–10V–2Fe–3Al alloy by Arrhenius equation, and predicted the dynamic restoration mechanism with determined average activation energy. Xu et al. [4] studied the deformation behavior of Ti-17 alloy with lamellar structure and concluded that dynamic globularization of α phase and continuous dynamic recrystallization (DRX) of β phase are two main factors for flow softening. Balachandran et al. [5] investigated the recrystallization behavior of Ti5553 alloy, and concluded that conventional recrystallization and epitaxial recrystallization operated simultaneously. Jia et al. [6]

^{*} Corresponding author: Xuemei Yang, School of Aerospace Engineering, Zhengzhou University of Aeronautics, Zhengzhou 450046, PR China, e-mail: yangxuemei@mail.nwpu.edu.cn, tel: +86 0371 61912068

suggested that increasing deformation temperature and strain is beneficial to the DRX process of powder metallurgy Ti–22Al–25Nb alloy. Quan et al. [7] analyzed the variation of DRX volume fraction with different deformation parameters of Ti–6Al–4V alloy. Li et al. [8] developed a series of variable-based unified viscoplastic constitutive models to represent the flow behavior and globularization evolution of TC6 alloy. Liu et al. [9] proposed an improved constitutive model of Ti–6Al–4V alloy incorporating DRX volume fraction as the internal state variable.

In this research, hot compression experiments of Ti-6.5Al-2Sn-4Zr-4Mo-1W-0.2Si alloy at different deformation temperatures and strain rates were carried out. Dynamic softening behaviors were identified by comparing saturated dislocation density with the critical density for DRX occurrence. Besides, on account of the experimental stresses corresponding to different deformation conditions, a piecewise physical-based model was established in view of the work hardening (WH) and dynamic softening behaviors. Finally, the microstructural evolution associated with different flow softening behaviors was analyzed.

2 Experimental materials and procedures

2.1 Sample preparation

The experimental material is supplied in a form of alloy rod with a diameter of 270 mm. Before hot deformation, the provided rod was sectioned into round bars with a dimension of \emptyset 15 mm \times 100 mm. Then, the specimens were thermally treated at 995°C for 30 min. Subsequently, the specimens were air cooled to room temperature. As shown in Figure 1, the microstructure is composed of totally basket-weave structure with lamellar α distributed disorderly on the β matrix.

2.2 Experimental procedures

The β phase transition temperature (T_{β}) of the studied Ti-6.5Al-2Sn-4Zr-4Mo-1W-0.2Si alloy was confirmed as 965°C by metallographic technique. Cylindrical specimens with the dimension of Φ 10 mm \times 15 mm and surface roughness of 1.6 μ m were prepared. Isothermal compression experiments were performed on a Gleeble-3500 thermosimulation machine at temperatures of 940, 970, 1,000, and 1,030°C, and strain rates of 0.001, 0.01, 0.1, 1, and

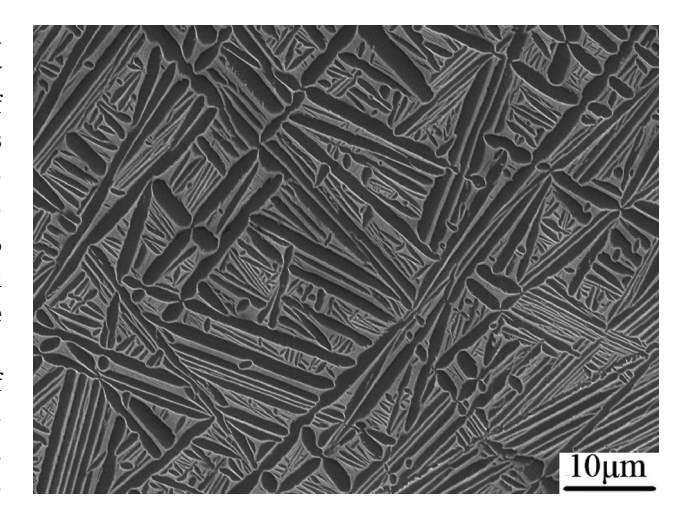


Figure 1: Lamellar starting microstructure of Ti-6.5Al-2Sn-4Zr-4Mo-1W-0.2Si alloy.

10 s⁻¹, respectively. All the specimens were compressed by 60% of the initial height. Lubricants like graphite powder were put between the specimens and anvils to reduce the friction during compression. Before hot deformation, the specimens were heated with a rate of 10°C·s⁻¹ and insulated for 5 min to obtain a uniform temperature distribution. During isothermal compression, the load-stroke curves can be recorded automatically and converted into true stress-strain curves. After hot deformation, the specimens were immediately water-quenched to room temperature to maintain the high-temperature deformed microstructure. To analyze the microstructural evolution, the specimens were axially cut, polished and etched by a solution consisting of HF $(3 \text{ mL}) + \text{HNO}_3 (6 \text{ mL}) + \text{H}_2\text{O} (91 \text{ mL})$. The microstructure was observed on the Olympus microscope, the TESCAN MIRA3 SEM and the Tecnai F30 G² field emission transmission electron microscope (TEM).

3 Results and discussion

3.1 Flow behavior

The high-temperature plastic deformation generally occurs along with the competition between work hardening and dynamic softening. Figure 2 presents typical flow curves of Ti–6.5Al–2Sn–4Zr–4Mo–1W–0.2Si alloy with different strain rates and deformation temperatures. Based on the values of work hardening rate θ (θ = d σ /d ε , σ and ε , respectively, denote the true stress and true strain measured on the flow curves), the flow curves can be separated into four typical stages. As can be observed from Figure 2(b), the flow

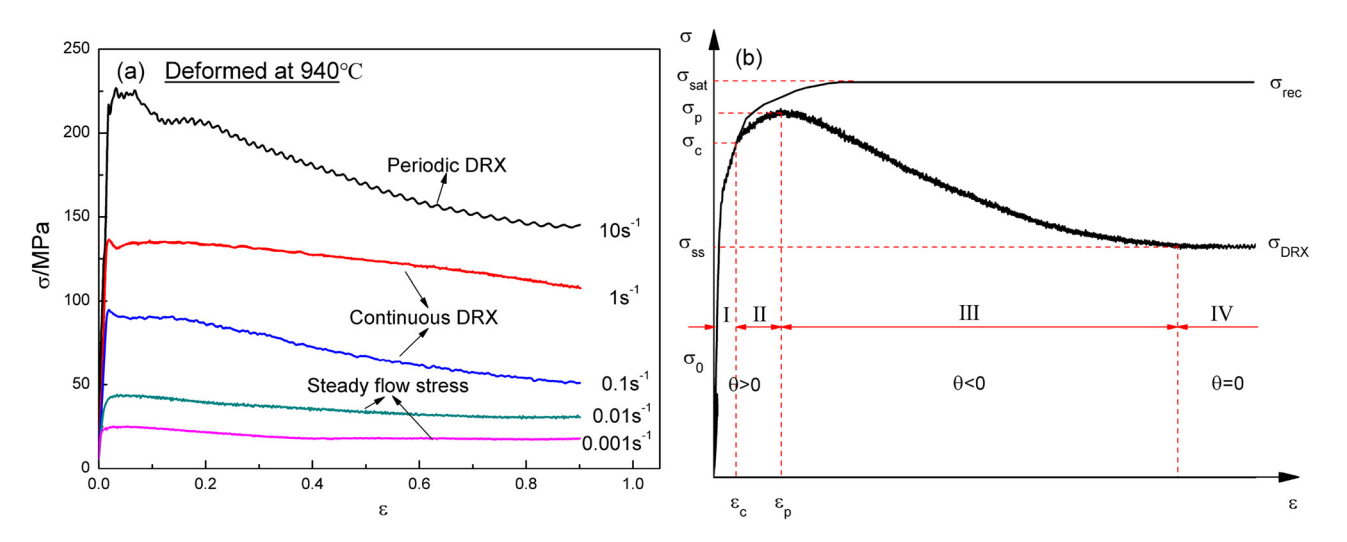


Figure 2: (a) True stress-strain curves of Ti-6.5Al-2Sn-4Zr-4Mo-1W-0.2Si alloy under different deformation conditions and (b) schematic diagram for different deformation stages illustrated on typical flow curves.

stress increases rapidly with small strain at the work hardening stage ($\theta > 0$), as a result of extensive dislocation proliferation and entanglement occurring due to work hardening [10]. When the strain surpasses the critical strain to activate DRX behavior, the flow stress continues to increase with a much smaller rate until reaching the peak value. Following the peak stress, the flow curves decrease gradually with the acceleration of DRX softening, which belongs to the dynamic softening stage ($\theta < 0$). Finally, when the work hardening and flow softening attain a dynamic equilibrium at large strain, the flow stresses become relatively stable and the flow curve turns into ultimate steady-state stage ($\theta = 0$) [11,12].

The true stress-strain curves can be categorized into three representative types based on the flow characteristics. When deformed at high strain rate of 10 s^{-1} , the flow curve presents the feature of multi peak stresses, and then decreases undulately with further deformation. This phenomenon might be attributed to the occurrence of periodic dynamic recrystallization (PDRX) [13]. The nucleation and growth of DRX grains would consume large amounts of dislocations, and thus significantly reduce the flow stress. Nevertheless, the continuous plastic deformation will promote the dislocation multiplication in newly formed recrystallized grains. Before the growth up of recrystallization grain, whether its dislocation density can achieve the critical value for DRX occurrence and lead to the next cycle of DRX behavior determines the flow features of true stress-strain curves. If the increasing dislocation density cannot achieve the critical value for DRX, a new round of work hardening would take into effect. Once the accumulated dislocation density exceeds the critical value, DRX will occur again. Thus, periodic jitter can be observed on

the true stress–strain curves with high strain rate of $10 \, \mathrm{s}^{-1}$. Conversely, if the dislocation density is always maintained beyond the critical value, DRX behavior will go on continuously by the progressive rotation of sub-grains with little accompanying boundary migration, and the flow curves show a feature of continuous decline after a single peak stress (deformed at strain rates of 1 and $0.1 \, \mathrm{s}^{-1}$), which is called continuous dynamic recrystallization (CDRX) [14–16]. Furthermore, another type of true stress–strain curve is characterized by steady flow. When deformed at lower strain rates of 0.01 and 0.001 $\, \mathrm{s}^{-1}$, the flow stress increases rapidly until reaching the maximum value, then the flow stress remains almost constant with further strain. There is no obvious peak stress on these flow curves.

3.2 Kinetic analysis

For metallic materials, the combined effects of deformation temperature and strain rate on the flow stress can be described by the Zener–Hollomon parameter (Z) [17]:

$$Z = \dot{\varepsilon} \exp(Q/RT) = A[\sinh(\alpha\sigma)]^n, \tag{1}$$

where $\dot{\varepsilon}$ is the strain rate (s⁻¹), σ is the true stress (MPa), R is the gas constant (8.3145 J·mol⁻¹·K⁻¹), T is the absolute temperature (K), Q is the deformation activation energy (kJ·mol⁻¹), n is the stress exponent, A and α are material constants.

Taking partial derivative of equation (1), n and Q can be calculated from the following equations:

$$n = \frac{\partial \ln \dot{\varepsilon}}{\partial \ln[\sinh(\alpha\sigma)]},\tag{2}$$

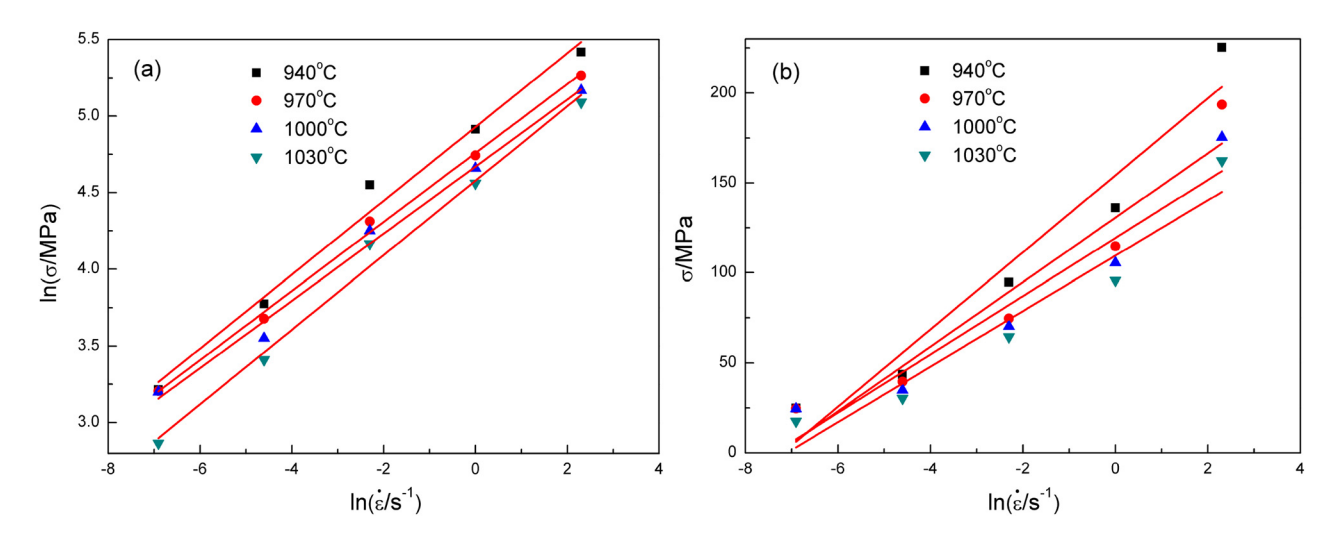


Figure 3: Linear regression analysis for the plots of: (a) $\ln \sigma - \ln \dot{\varepsilon}$ and (b) $\sigma - \ln \dot{\varepsilon}$.

$$Q = Rn \frac{\partial \ln[\sinh(\alpha \sigma)]}{\partial (1/T)}.$$
 (3)

Flow stresses corresponding to different peak strains are substituted into above equations. The constant α is calculated as 0.0131 from the linear fitting of $\ln \dot{\varepsilon} - \ln \sigma$ plot and $\ln \dot{\varepsilon} - \sigma$ plot in Figure 3. The average values of n and Q are calculated as 3.1256 and 237.01 kJ·mol⁻¹ from the fitting plots of $\ln \dot{\varepsilon} - \ln[\sinh(\alpha\sigma)]$ and $\ln[\sinh(\alpha\sigma)]$ –1,000/T, respectively, as shown in Figure 4.

The thermal activation process of titanium alloys vitally influences the softening mechanism. The calculated Q value is quite larger than the $Q_{\rm sef}$ (self-diffusion energy) for both α -Ti (169 kJ·mol⁻¹) and β -Ti (153 kJ·mol⁻¹), precluding diffusion playing a major role in the hot deformation, and indicating that DRX is very likely to happen [18].

Figure 5 shows the linear correlation between $\ln Z$ and $\ln[\sinh(\alpha\sigma)]$. The value of $\ln A$ is calculated as 19.910.

Thus, the peak stress σ_p can be described as a mathematical relationship of Zener–Hollomon parameter:

$$\sigma_{\rm p} = \frac{1}{\alpha} \ln \left\{ \left(\frac{Z}{A} \right)^{1/n} + \left[\left(\frac{Z}{A} \right)^{2/n} + 1 \right]^{1/2} \right\}.$$
 (4)

3.3 Constitutive modeling of flow stress

3.3.1 Identification of dynamic softening behavior

It is well known that both dynamic recovery (DRV) and DRX softening behaviors can lead to the decrease in dislocation density and thus the flow stress. Suppose that the deformation dynamics is mainly controlled by dislocation density ρ , Mecking and Kocks [19] proposed a novel model (K–M model) to describe the variation of dislocation density

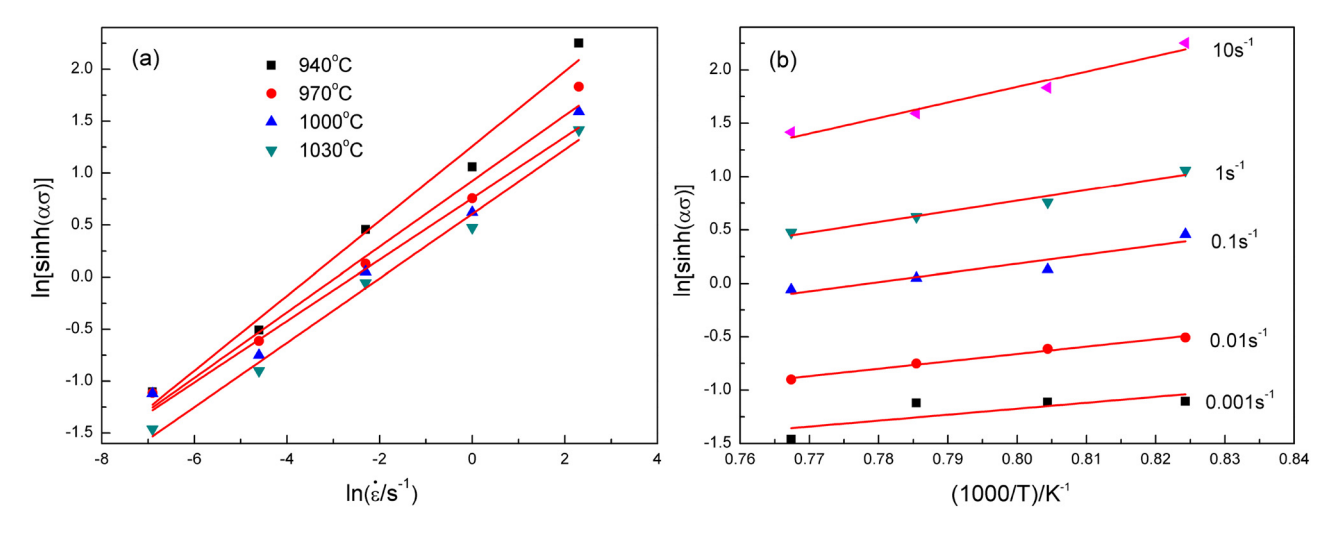


Figure 4: Linear regression analysis of (a) $\ln[\sinh(\alpha\sigma)] - \ln \dot{\epsilon}$ and (b) $\ln[\sinh(\alpha\sigma)] - 1,000/T$.

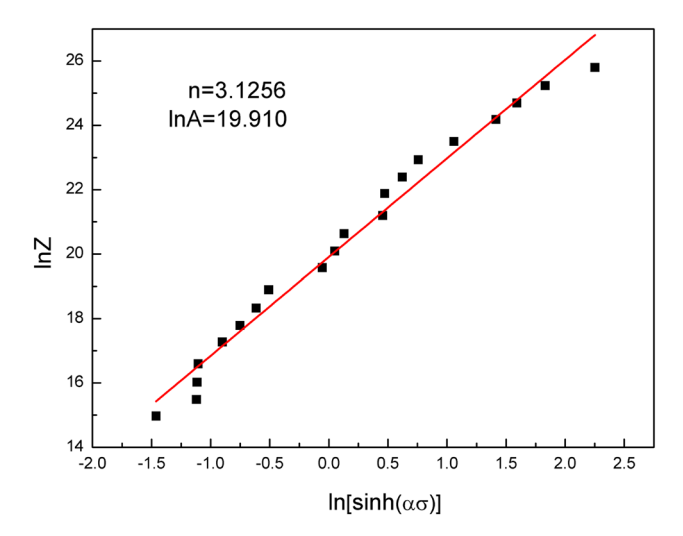


Figure 5: Linear regression analysis for the $\ln Z - \ln[\sinh(\alpha\sigma)]$ plot.

during hot deformation. According to the free path that dislocation can move on a glide plane [20], the dislocation multiplication rate resulted from work hardening is linearly related to $\sqrt{\rho}$. Based on the first-order dynamics, the dislocation annihilation rate due to dynamic recovery is in proportion to ρ [21]. Thus, the dislocation evolution at WH and DRV stage could be summarized as follows:

$$\frac{\mathrm{d}\rho}{\mathrm{d}\varepsilon} = k_1 \sqrt{\rho} - k_2 \rho,\tag{5}$$

where $d\rho/d\varepsilon$ denotes the variation rate of dislocation density. k_1 determines the dislocation multiplication rate, which is related to the material structural characteristics. k_1 could be calculated using the following formula [22]:

$$k_1 = \frac{2\theta_{\Pi}}{\beta G b},\tag{6}$$

where $\theta_{\rm II}$ denotes the flow curve slope in stage II, $\sim G/200$. β is the Taylor constant, ~ 0.5 . G is the shear modulus, ~ 44 GPa. D is the magnitude of Burgers vector, $\sim 2.86 \times 10^{-10}$ m⁻¹ [23].

The rate of dislocation annihilation is determined by k_2 and can be achieved by dislocation glide, climb and cross-slip during DRV process. k_2 can be calculated by ref. [24]

$$k_2 = k\beta \text{MG}b(k_1/\sigma_{\text{n}}), \tag{7}$$

where k is the proportional constant, M is the Taylor conversion factor from shear strain r to normal strain ε , ~3.06. $\sigma_{\rm p}$ is the peak stress which could be obtained through equation (4) or directly measured on the true stress–strain curves.

The saturated stress $\sigma_{\rm sat}$ represents the maximum hardening capacity when the dynamic competition between dislocation multiplication rate from work hardening and dislocation annihilation rate from DRV softening achieve balance [25]. Therefore, once the flow stress reaches saturated stress, corresponding dislocation variation rate $d\rho/d\epsilon$ falls to zero, and relevant saturated dislocation density $\rho_{\rm sat}$ can be calculated from equation (5) as

$$\frac{\mathrm{d}\rho_{\mathrm{sat}}}{\mathrm{d}\varepsilon} = k_1 \sqrt{\rho_{\mathrm{sat}}} - k_2 \rho_{\mathrm{sat}} = 0 \text{ with } \rho_{\mathrm{sat}} = \left(\frac{k_1}{k_2}\right)^2. \tag{8}$$

According to the thermodynamic transformation of DRX mechanism, Varshni [26] put forward a model to quantify the critical dislocation density $\rho_{\rm c}$ for DRX occurrence. $\rho_{\rm c}$ can be calculated as

$$\rho_{\rm c} = \left(\frac{20\gamma\dot{\varepsilon}}{3b^5lG^2M_{\rm bm}}\right)^{1/3},\tag{9}$$

where y denotes the boundary energy, l is the average free distance of dislocations generally taken as $3\sim5b$ [27]. $M_{\rm bm}$ is the boundary mobility and could be obtained by the following equation [28]:

$$M_{\rm bm} = \frac{\delta D_{\rm b} b}{kT} \text{ with } D_{\rm b} = D_0 \cdot \exp\left(-\frac{Q_{\rm b}}{RT}\right),$$
 (10)

where δ is the characteristic grain boundary thickness, $D_{\rm b}$ represents the self-diffusivity along grain boundary. $Q_{\rm b}$ is the boundary diffusion activation energy which is taken as $150~{\rm kJ\cdot mol^{-1}}$, k is Boltzmann's constant, $\sim 1.381\times 10^{-23}~{\rm J\cdot K^{-1}}$.

During hot deformation, DRX behavior can only be activated once the accumulated dislocation density within deformed grains achieves the critical value for DRX occurrence. Therefore, the identification of dynamic softening behavior from dislocation evolution can be expressed as:

$$ho_{\rm sat} \ge
ho_{\rm c} \Rightarrow \left(rac{1.12\sigma_{
m p}}{eta MGb}
ight)^2 \ge \left(rac{20y\dot{\epsilon}}{3b^5lG^2M_{
m bm}}
ight)^{1/3} \Rightarrow {
m DRX},$$

$$\rho_{\rm sat} < \rho_{\rm c} \Rightarrow \left(\frac{1.12\sigma_{\rm p}}{\beta MGb}\right)^2 < \left(\frac{20\gamma\dot{\varepsilon}}{3b^5lG^2M_{\rm bm}}\right)^{1/3} \Rightarrow {\rm DRV}, (11)$$

Figure 6(a) and (b) presents the comparisons between calculated $\rho_{\rm sat}$ and $\rho_{\rm c}$ under different deformation conditions. The comparisons are conducted at typical temperatures below and above the β phase transition temperature, respectively. As can be seen, with the increase of strain rate, $\rho_{\rm sat}$ and $\rho_{\rm c}$ increase simultaneously, but relationships between the two parameters corresponding to different strain rates are not exactly the same. For lower strain rates of 0.001 and $0.01\,{\rm s}^{-1}$, both $\rho_{\rm sat}$ and $\rho_{\rm c}$ are much small, which corresponds to steady flow on the true stress—strain curves. As for strain rates of 0.1 and $1\,{\rm s}^{-1}$, $\rho_{\rm sat}$ is much larger than $\rho_{\rm c}$, thus CDRX behavior occurs easily under these deformation conditions, resulting in continuous decline after peak stress on the flow curves. With further increase of strain rate, the increasing rate of $\rho_{\rm c}$ becomes much larger

than that of $\rho_{\rm sat}$, and the $\rho_{\rm c}$ at strain rate of 10 s⁻¹ has almost caught up with $\rho_{\rm sat}$, thus PDRX behavior occurs at such a high strain rate. The dynamic softening behaviors can also be identified by the Poliak–Jonas criterion from nonequilibrium thermodynamic perspective. The occurrence of DRX behavior can be figured out by the inflection points on work-hardening $(\theta-\sigma)$ curves or the minimum points on $(-\partial\theta/\partial\sigma)$ curves [29]. As Figure 6(c) and (d) show, minimum points can almost be observed on each $-\partial\theta/\partial\sigma$ curve, which validates the occurrence of DRX under these conditions.

3.3.2 Constitutive model of the work-hardening and dynamic recovery stage

The variation of dislocation density is largely influenced by the competition between work hardening at small strains and dynamic softening at larger strains. Generally, the relationship between dislocation density and plastic strain can be presented as follows [30]:

$$\frac{\mathrm{d}\rho}{\mathrm{d}\varepsilon} = U - \Omega\rho,\tag{12}$$

where U denotes the influence of work hardening resulted from dislocation multiplication, entanglement and pile-up, which is irrelevant to the strain and can be considered as a constant. $\Omega\rho$ signifies the influence of DRV softening caused by dislocation offset and rearrangement.

Taking integration of equation (12), the dislocation density ρ can be calculated as follows:

$$\rho = \frac{U}{\Omega} - \left(\frac{U}{\Omega} - \rho_0\right) e^{-\Omega \varepsilon}, \tag{13}$$

where ρ_0 is the initial dislocation density.

On account of the Taylor relation, flow stress σ can be represented as the function of dislocation density ρ [31]

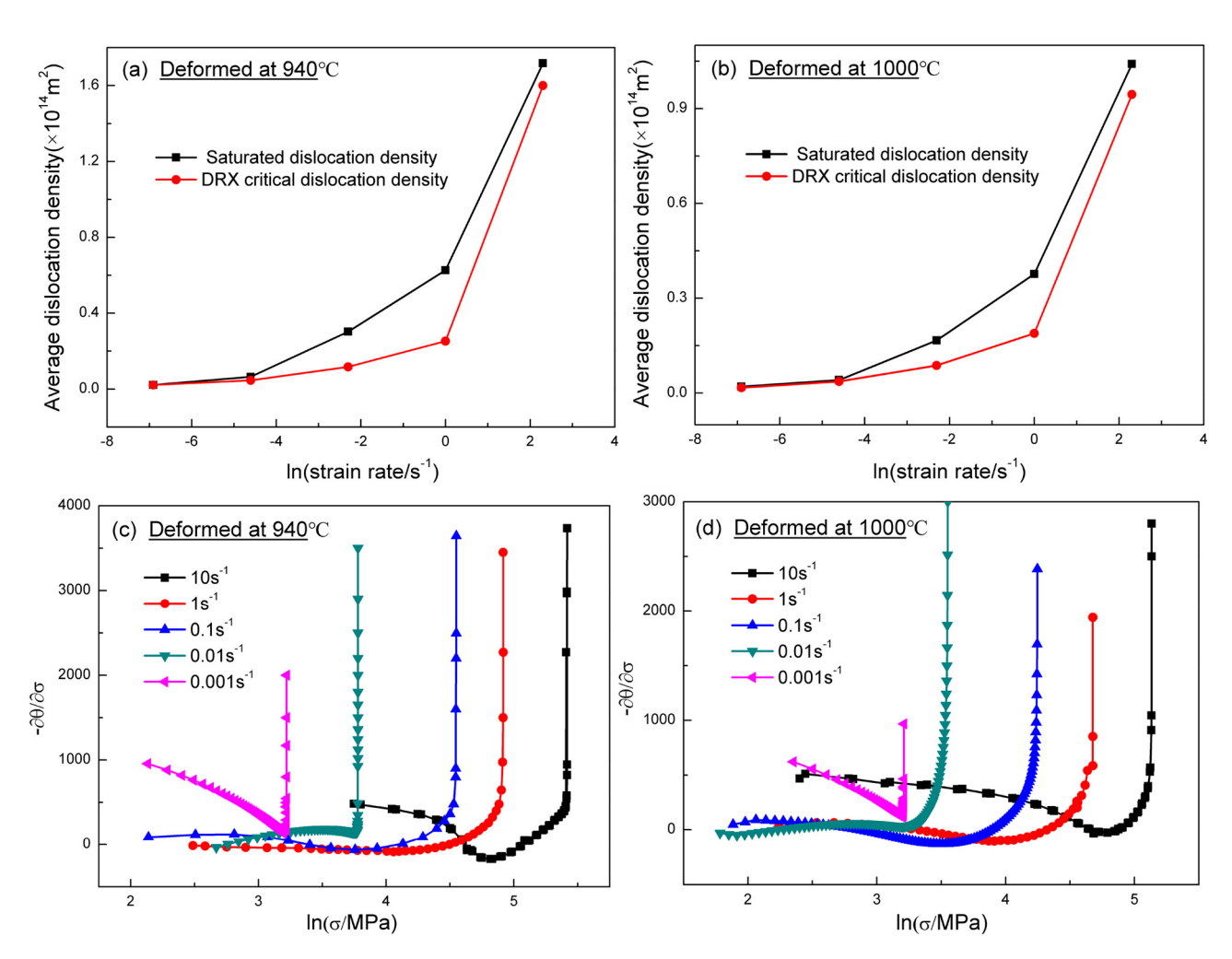


Figure 6: Comparisons between ρ_{sat} and ρ_{c} , and verification of the dynamic softening behavior through Poliak–Jonas criterion under different deformation conditions of (a and c) 940°C and (b and d) 1,000°C.

$$\sigma = \beta M G b \sqrt{\rho} \,, \tag{14}$$

By substituting equation (14) into equation (13), the flow stress σ during WH and DRV stage could be calculated by the following formula:

$$\sigma = \left[\sigma_{\text{sat}}^2 + (\sigma_0^2 - \sigma_{\text{sat}}^2)e^{-\Omega\varepsilon}\right]^{0.5} (\varepsilon < \varepsilon_c), \tag{15}$$

where the saturation stress $\sigma_{\rm sat}$ and yield stress σ_0 are equal to $\alpha MGb\sqrt{U/\Omega}$ and $\alpha MGb\sqrt{\rho_0}$, respectively.

The variable $\sigma_{\rm sat}$ has been considered as the maximum hardening capacity with mainly DRV softening, and could be obtained once the work hardening rate $\theta_{\rm DRV}$ reaches zero.

$$\theta_{\rm DRV} = \frac{\partial \sigma_{\rm DRV}}{\partial \varepsilon} = 0. \tag{16}$$

Combining equation (14) with equation (5), the work hardening rate θ_{DRV} can be expressed by the linear function of flow stress σ .

$$\theta_{\rm DRV} = \frac{\beta MGbk_1}{2} - \frac{k_2}{2}\sigma. \tag{17}$$

As equation (17) describes, the $\theta_{\rm DRV}$ value during WH and DRV stage is correlated linearly with the flow stress σ , which is in accordance with the work-hardening curve shown in Figure 7. Generally, the saturated stress $\sigma_{\rm sat}$ could be directly measured by the abscissa intercept of the tangent line of θ - σ curve through the inflection point [32]. More accurately, the $\sigma_{\rm sat}$ value can be calculated by the combination of equations (6), (7), and (16) as follows:

$$\sigma_{\text{sat}} = \beta MGbk_1/k_2 = k \cdot \sigma_{\text{p}}, \tag{18}$$

where the proportional coefficient k has the same meaning as the constant in equation (7), which is presented in

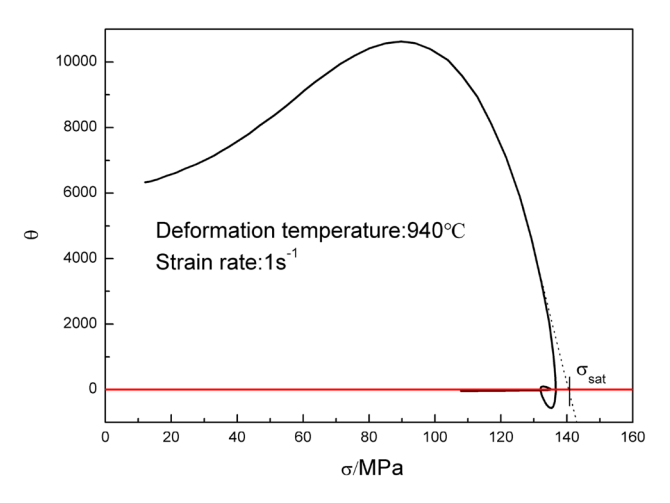


Figure 7: Relationship between the work hardening rate θ and flow stress σ at certain deformation condition and determination of $\sigma_{\rm sat}$ value on the θ - σ curve.

Figure 8. Thus, the quantitative relation between σ_{sat} and σ_{p} can be expressed as

$$\sigma_{\text{sat}} = 1.0427\sigma_{\text{p}}.\tag{19}$$

The yield stress σ_0 corresponding to different deformation conditions can be measured on the true stress-strain curves. As Figure 9 shows, $\ln \sigma_0$ and $\ln Z$ are linearly dependent. Thus, the σ_0 value can be represented by the Zener–Hollomon parameter as follows:

$$\sigma_0 = 2.6218Z^{0.0969}. (20)$$

The dynamic recovery coefficient Ω could be obtained from equation (15) as

$$\Omega \varepsilon = \ln \left(\frac{\sigma_{\text{sat}}^2 - \sigma_0^2}{\sigma_{\text{sat}}^2 - \sigma^2} \right). \tag{21}$$

On account of the stress values measured on the flow curves before critical strain, the values of Ω corresponding to different temperatures and strain rates can be calculated. As can be observed in Figure 10, the values of $\ln \Omega$ present a linear relationship with $\ln Z$. Thus, Ω can be expressed as:

$$\Omega = 652.4405Z^{-0.085}. (22)$$

3.3.3 Constitutive model of the DRX stage

With further deformation, flow softening behavior gradually dominates. Once the accumulated distortion storage and dislocation density reach critical conditions, rearrangement and polygonization of dislocations would contribute to the formation of sub-structures, which become nuclei of DRX grains. Then, non-distorted recrystallized

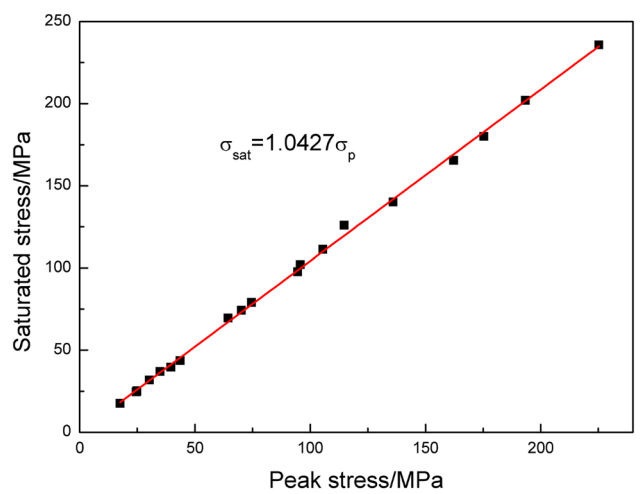


Figure 8: Relationship between $\sigma_{\rm sat}$ and $\sigma_{\rm p}$.

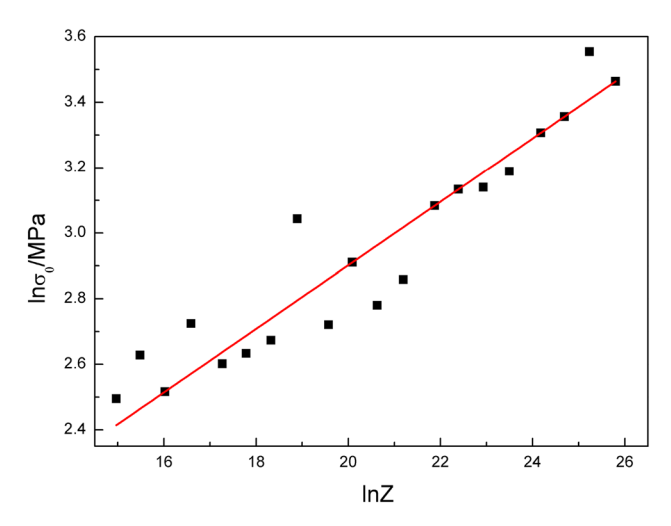


Figure 9: Linear dependence between $\ln \sigma_0$ and $\ln Z$.

grains nucleate and grow up gradually with grain boundary migration [33]. The increase rate of flow stress on the flow curves would decelerate and turn downward gradually with the DRX occurrence, as shown in Figure 2. The DRX kinetics could be expressed by the Avrami equation as [34]

$$X_{\text{DRX}} = 1 - \exp \left[-K_{\text{d}} \left(\frac{\varepsilon - \varepsilon_{\text{c}}}{\varepsilon_{\text{p}}} \right)^{n_{\text{d}}} \right], \quad (\varepsilon \ge \varepsilon_{\text{c}}), \quad (23)$$

where $\varepsilon_{\rm p}$ is the peak strain which could be measured on the true stress–strain curves, $\varepsilon_{\rm c}$ is the critical strain for DRX occurrence, $\varepsilon_{\rm c}=0.85\varepsilon_{\rm p}$. $K_{\rm d}$ and $n_{\rm d}$ are DRX parameters. Generally, there is a specific relationship between $X_{\rm DRX}$ and flow stress σ as [35] follows:

$$X_{\text{DRX}} = \frac{\sigma_{\text{DRV}} - \sigma}{\sigma_{\text{sat}} - \sigma_{\text{ss}}}, \quad (\varepsilon \ge \varepsilon_{\text{c}}),$$
 (24)

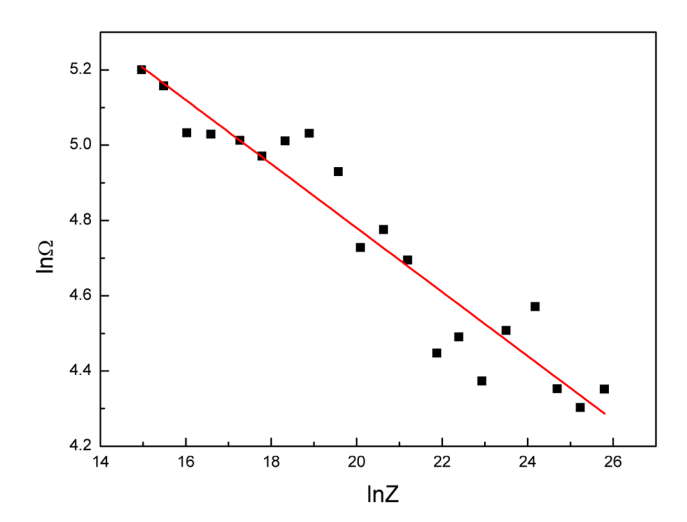


Figure 10: Linear dependence between $\ln \Omega$ and $\ln Z$.

where $\sigma_{\rm DRV}$ denotes the flow stress while DRV softening occupies a major part, which can be obtained from equation (15). σ represents the flow stress corresponding to certain strain ε on the flow curves in Figure 2. $\sigma_{\rm sat}$ is the saturated stress when work hardening and DRV softening achieve the balance, which has been discussed in Section 3.3.2.

The steady stress σ_{ss} results from the dynamic balance between work hardening and DRX softening, which could be directly measured at relatively large strains on the true stress–strain curves [36]. In this study, stresses at strain of 0.7 were adopted as the σ_{ss} values. As observed in Figure 11, the steady stress σ_{ss} almost keeps linear with the peak stress σ_{p} . Thus, σ_{ss} can be expressed as follows:

$$\sigma_{\rm ss} = 0.7730\sigma_{\rm p}.\tag{25}$$

Substituting equation (24) into equation (23), the flow stress σ during DRX stage could be calculated as:

$$\sigma = \sigma_{\text{DRV}} - (\sigma_{\text{sat}} - \sigma_{\text{ss}}) \left\{ 1 - \exp \left[-K_{\text{d}} \left(\frac{\varepsilon - \varepsilon_{\text{c}}}{\varepsilon_{\text{p}}} \right)^{n_{\text{d}}} \right] \right\}, \quad (\varepsilon \ge \varepsilon_{\text{c}}).$$
 (26)

Figure 12 presents the relationship between $\ln[-\ln (1-X_{DRX})]$ and $\ln[(\varepsilon-\varepsilon_c)/\varepsilon_p]$. By taking the least squares method, data drawn in the coordinate system is linearly fitted. Then, the mean values of K_d and n_d are achieved as 0.0471 and 1.1551, respectively.

3.3.4 Verification of established constitutive models

Figure 13 presents the comparison between predicted and experimental flow curves of Ti-6.5Al-2Sn-4Zr-4Mo-1W-0.2Si

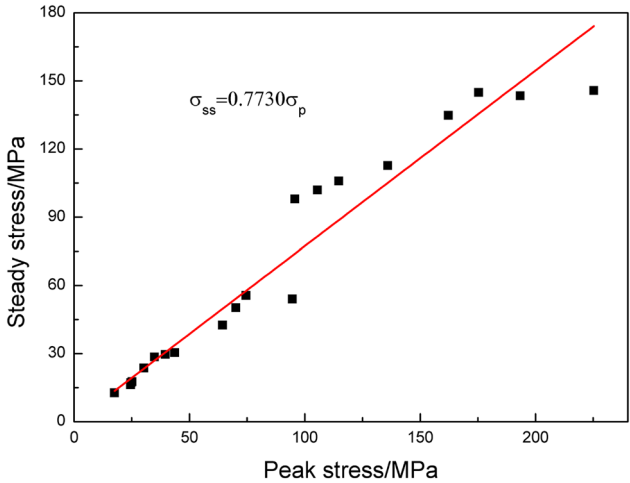


Figure 11: Linear dependence between σ_{ss} and σ_{p} .

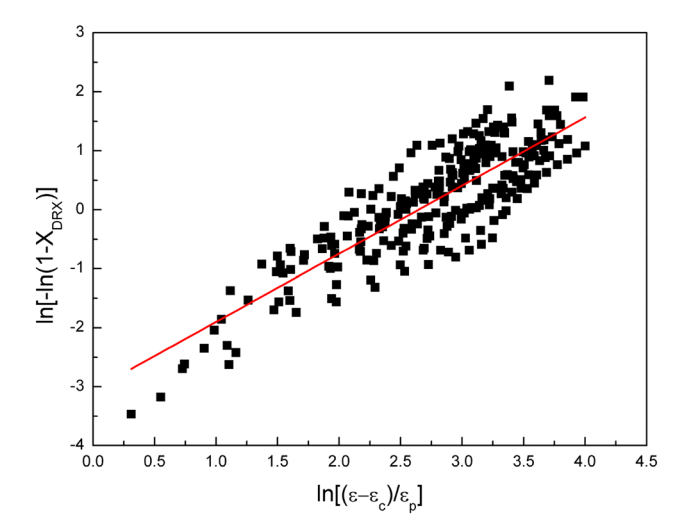


Figure 12: Linear dependence between $\ln[-\ln(1-X_{DRX})]$ and $\ln[(\varepsilon-\varepsilon_c)/\varepsilon_p]$.

alloy at deformation temperatures of $940-1,030^{\circ}$ C and strain rates of $0.001-10 \text{ s}^{-1}$. It suggests that the predicted stresses are in good accordance with the experimental ones. However,

small deviations can be observed within a short strain range after crossing the peak stress when deformed at high strain rates. As can be seen from Figure 14, adiabatic shear band is distributed along the direction 45° to the compressive axis. While deformed at high strain rate, the adiabatic deformation heat generated in the central part of the specimens cannot be conducted out on time because of insufficient deformation time and low thermal conductivity, resulting in a significant flow softening on the experimental true stress–strain curves [37]. Thus, the predicted flow stresses are higher than the experimental stresses for high strain rate deformation.

In order to further evaluate the predictive precision of developed constitutive model, the scatter map of experimental and predicted flow stresses under all deformation conditions is shown in Figure 15. It can be seen that the predicted stresses match well with the experimental ones. Moreover, the correlation coefficient *R* and average absolute relative error (AARE) are calculated as 0.9866 and 5.03%, respectively, suggesting good predictive capability of the developed model.

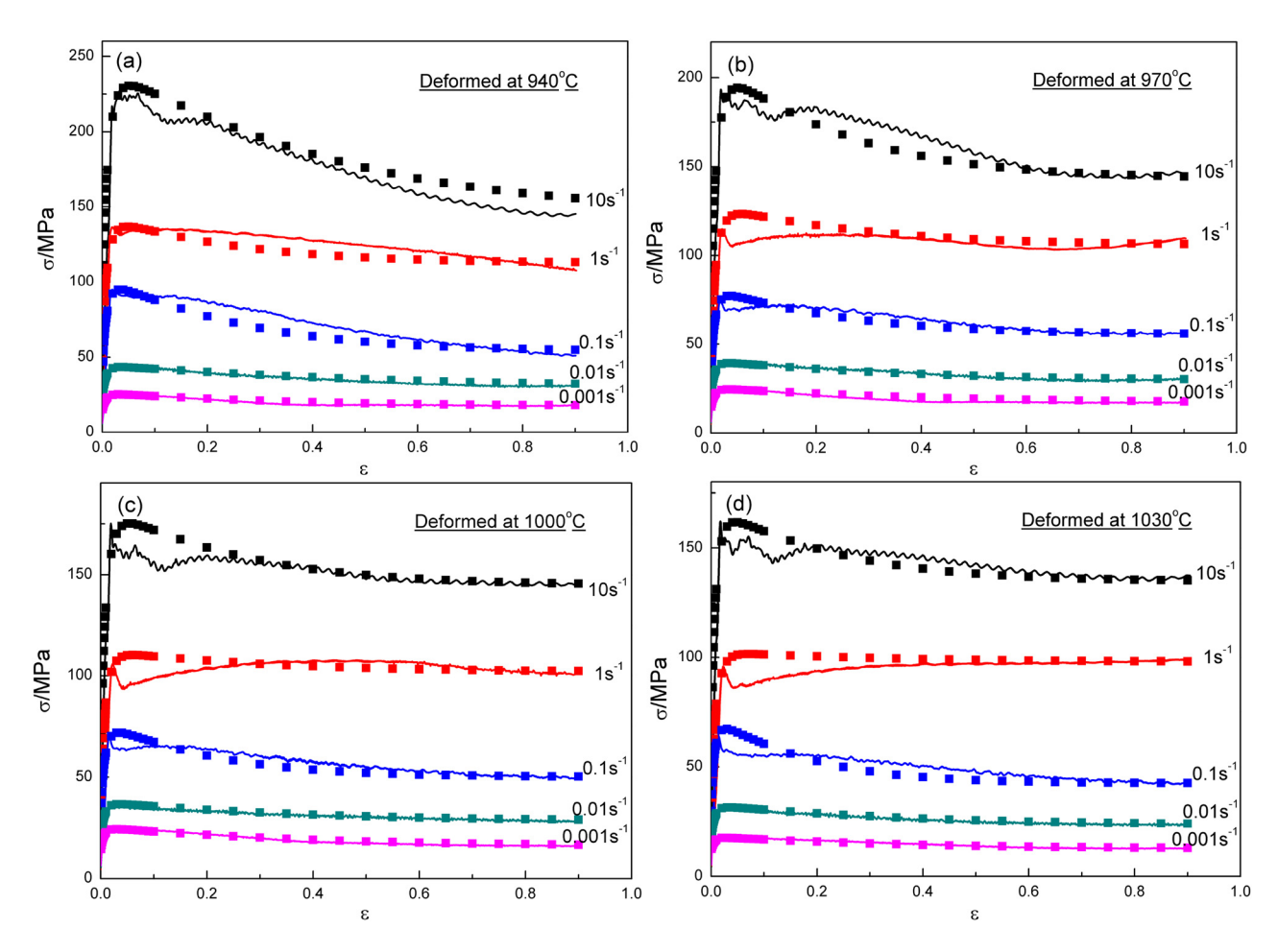


Figure 13: Comparison between predicted and experimental flow curves at temperatures of: (a) 940°C; (b) 970°C; (c) 1,000°C; and (d) 1,030°C (the curves represent experimental results and symbols represent predicted ones).



Figure 14: Adiabatic shear band observed at high strain rate of 10 $\rm s^{-1}$.

$$R = \frac{\sum_{i=1}^{N} (X_i - \bar{X})(Y_i - \bar{Y})}{\sqrt{\sum_{i=1}^{N} (X_i - \bar{X})^2} \sqrt{\sum_{i=1}^{N} (Y_i - \bar{Y})^2}},$$
 (27)

AARE =
$$\frac{1}{N} \sum_{i=1}^{N} \left| \frac{Y_i - X_i}{X_i} \right| \times 100\%,$$
 (28)

where X_i is the experimental flow stress and Y_i is the predicted flow stress gained from the established constitutive model. \bar{X} and \bar{Y} are mean values of the experimental flow

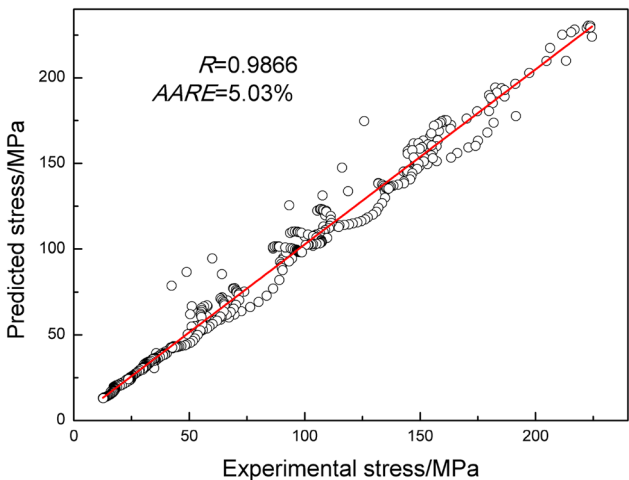


Figure 15: Correlation between predicted stress and experimental stress.

stress and predicted flow stress, respectively. *N* is the total number of stress data used in this study.

3.4 Microstructural evolution

The most effective and direct means to identify dynamic softening behaviors is microstructure observation, which

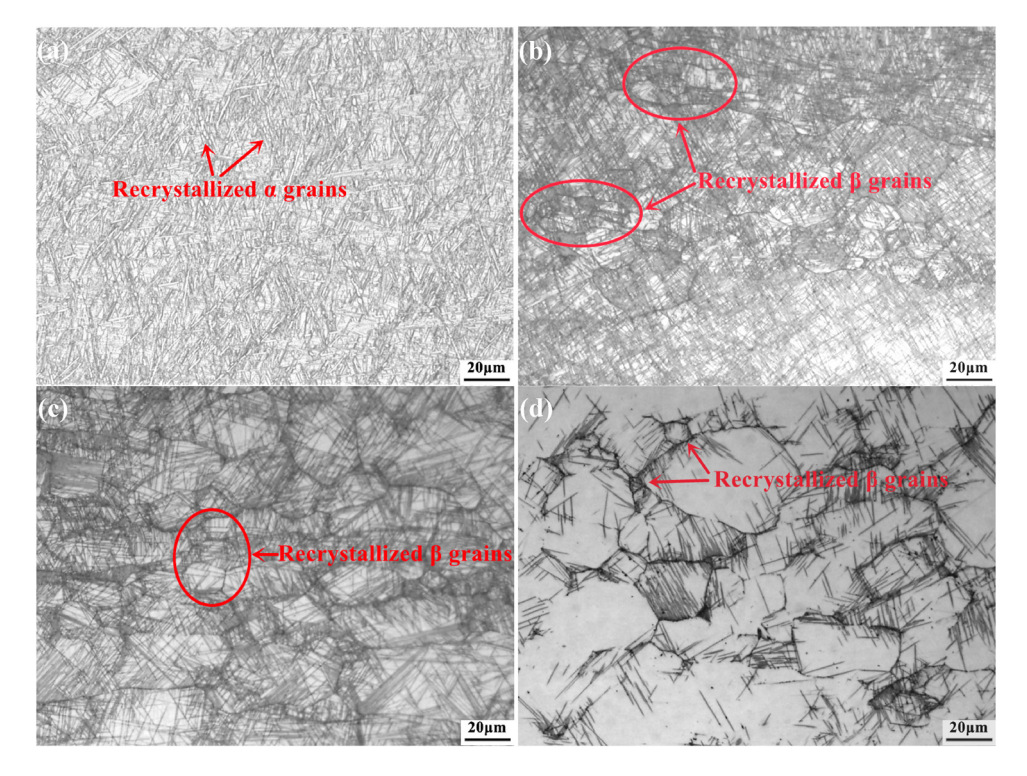


Figure 16: Microstructures after deformation at the same strain rate of $0.1 \, \text{s}^{-1}$ and different temperatures of (a) $940 \, ^{\circ}\text{C}$; (b) $970 \, ^{\circ}\text{C}$; (c) $1,000 \, ^{\circ}\text{C}$; and (d) $1,030 \, ^{\circ}\text{C}$.

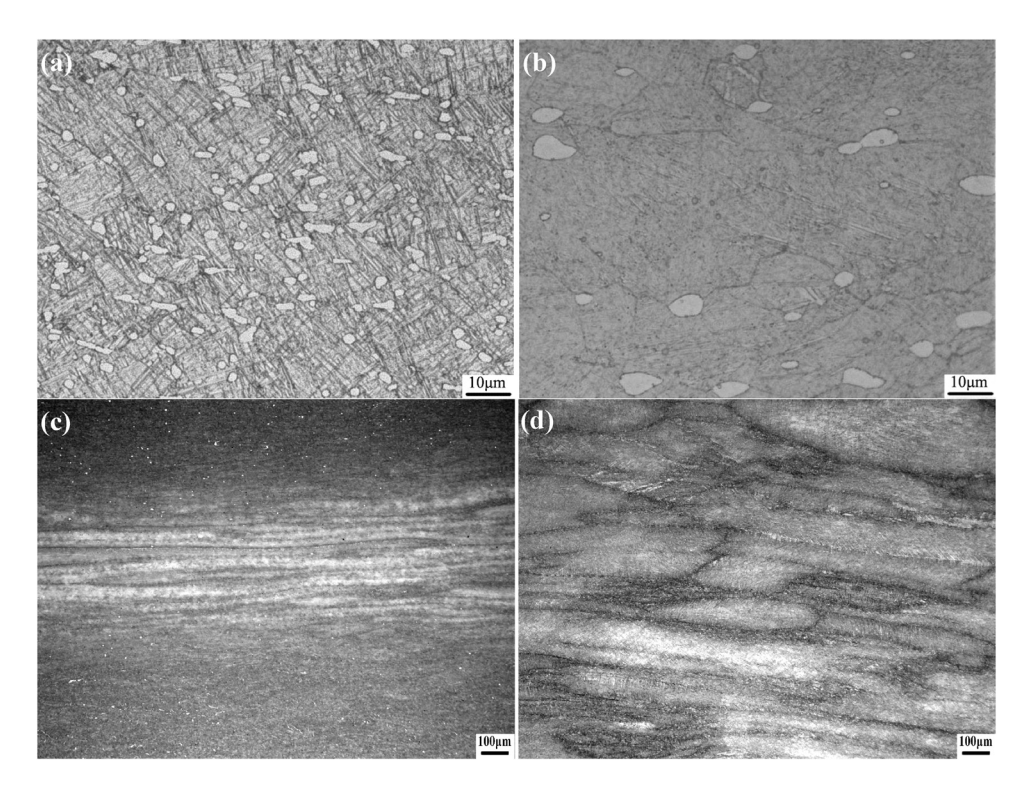


Figure 17: Microstructures after deformation at the same temperature of 940°C and different strain rates of (a) $0.001 \, \text{s}^{-1}$; (b) $0.01 \, \text{s}^{-1}$; (c) $1 \, \text{s}^{-1}$; and (d) $10 \, \text{s}^{-1}$.

could be used to judge the reliability of the proposed identification criterions. In general, the appearance of equiaxed or spheroidized grains in the deformed region is widely regarded as the representative characteristic of DRX behavior.

Figure 16 shows the effect of deformation temperature on the microstructure of Ti–6.5Al–2Sn–4Zr–4Mo–1W–0.2Si alloy at medium strain rate of $0.1\,\mathrm{s}^{-1}$. When deformed at temperature of 940°C in α + β phase region, there are a certain amount of fine equiaxed α grains in the microstructure, indicating DRX

mechanism plays a part in α phase. While deformed at 970°C above the β -transus temperature, the microstructure is totally composed of transformed β precipitated by interweaved acicular α . The prior- β grains are severely elongated and distributed vertical to the compression direction. Moreover, a few recrystallized β grains generate at the triple grain boundaries, as the red circle in Figure 16(b) shows. As the deformation temperature reaches 1,000°C, the grain boundary becomes much clear with good integrity, and necklace structures composed of a quite a number of small

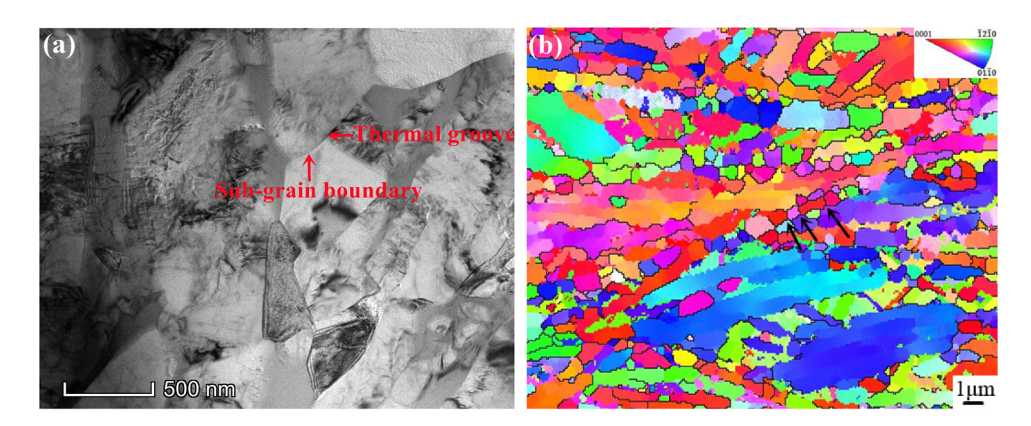


Figure 18: The morphology of substructure within lamellar α : (a) thermal groove and sub-grain boundary observed by TEM and (b) separation of lamellar α observed by electron backscatter diffraction.

equiaxed β grains distributes along the elongated prior- β grains, indicating that DRX behavior exists in the β phase. The microstructure characteristic of 1,030°C is almost the same with that of 1,000°C, only β grains and secondary lamellar α get further coarsened. Thus, DRX softening behavior occurs at all deformation temperatures but in α phase and β phase, respectively, while deformed below and above the β phase transition temperature.

Figure 17 shows the effect of strain rate on the microstructure while deformed at 940°C. When deformed at low strain rate of $0.001 \, \mathrm{s}^{-1}$, initial lamellar α have almost been totally broken into equiaxed a grains and get further coarsened. During hot deformation, the initial lamellar a become kinked and sub-grain boundaries generate as a result of dislocation rearrangement, as shown in Figure 18(a). With further deformation, the sub-grain boundaries transform into high-angle boundaries (HABs) by absorbing dislocation continuously, as indicated by the black arrows in Figure 18(b). Then, the β phase wedges into lamellar α along the HABs, and thermal groove generates at the junction between HABs and α/β phase boundaries. With the increase of groove depth, initial lamellar α grains are broken up and separated with short α lamellae. Finally, the fragmented α lamellae get globularization under the driving force of surface energy minimization [38]. While the strain rate rises to $0.01\,\mathrm{s}^{-1}$, most of the thick α lamellae get dynamic globularization and transform into equiaxed a grains. Besides, the quantity of equiaxed α grains decreases but grain size increases when compared with those of lower strain rate. As the strain rate increases to 1 s⁻¹, local plastic flow occurs in the β phase and fiber texture can be observed at the central part of the specimen. However, a few equiaxed α grains could still be observed in the region away from the large deformation zone, indicating that DRV in β phase and DRX in α phase work simultaneously. Once the strain rate reaches 10 s⁻¹, prior-β grains get seriously squashed along the metal flow direction. Moreover, there is almost no equiaxed α grains in the microstructure because of deformation heat existing in high strain rate. The DRX characteristics are not obvious in the non-uniform microstructure with local plastic flow and adiabatic shear band. Besides, the reduced deformation time hinders atom diffusion and dislocation climb which play an important role in the occurrence of DRX behavior, thus the corresponding softening behavior is PDRX mechanism.

4 Conclusion

The high-temperature flow behavior of Ti-6.5Al-2Sn-4Zr-4Mo-1W-0.2Si alloy with initial lamellar structure was

studied through isothermal compression tests. According to the description of flow behavior, kinetic analysis, constitutive establishment, and microstructure observation, several conclusions could be drawn as follows:

- (1) Multiple peaks on flow curves and microstructure inhomogeneity under high strain rate of 10 s⁻¹ have been identified as the PDRX behavior. Single peak and grain refinement at medium strain rates of 1 and 0.1 s⁻¹ are the characteristics of CDRX mechanism. Steady flow following the peak stress and grain coarsening appear at lower strain rates of 0.01 and 0.001 s⁻¹.
- 2) The deformation activation energy Q is calculated as 273.01 kJmol⁻¹, indicating the occurrence of DRX softening. The relationship between σ_p and Z parameter

is expressed as:
$$\sigma_{\rm p} = \frac{1}{\alpha} \ln \left\{ \left(\frac{Z}{A} \right)^{1/n} + \left[\left(\frac{Z}{A} \right)^{2/n} + 1 \right]^{1/2} \right\},$$

- where α , n, and $\ln A$ are calculated as 0.0131, 3.1256, and 19.910, respectively.
- (3) Dynamic softening behaviors have been determined by the comparison between $\rho_{\rm sat}$ and $\rho_{\rm c}$, and verified by the Poliak–Jonas criterion and microstructure observation. A piecewise physical-based constitutive model has been established to describe flow characteristics of the WH-DRV stage and DRX stage, respectively.

Funding information: This study was financially supported by the National Natural Science Foundation of China (No. 51904276), the Key Scientific Research Project of Colleges and Universities in Henan Province (No. 20A430032) and Key R&D and Promotion Special Project of Henan Province (No. 222102220093).

Author contributions: Conceptualization, H.Z. Guo; experiment, X.N. Shi; data processing, X.W. Yan; writing—original draft preparation, X.M. Yang; writing—review and editing, J.H. Zhao. All authors have read and agreed to the published version of the manuscript.

Conflict of interest: Authors state no conflict of interest.

Data availability statement: The data presented in this work are available on request from the corresponding authors.

References

[1] Yang, X. M., Z. L. Zhao, Y. Q. Ning, H. Z. Guo, H. Li, S. C. Yuan, et al. Microstructural evolution and mechanical property of isothermally forged BT25y titanium alloy with different double-

- annealing processes. *Materials Science & Engineering, A: Structural Materials: Properties, Microstructure and Processing*, Vol. 745, 2019, pp. 240–251.
- [2] Wang, K. X., W. D. Zeng, Y. Q. Zhao, Y. J. Lai, and Y. G. Zhou. Dynamic globularization kinetics during hot working of Ti-17 alloy with initial lamellar microstructure. *Materials Science & Engineering, A: Structural Materials: Properties, Microstructure and Processing*, Vol. 527, No. 10–11, 2010, pp. 2559–2566.
- [3] Zyguła, K., M. Wojtaszek, T. Śleboda, O. Lypchanskyi, M. Rumiński, G. Korpała, et al. The analysis of hot deformation behavior of powder metallurgy Ti-10V-2Fe-3Al alloy using activation energy and Zener-Hollomon parameter. *Procedia Manufacturing*, Vol. 50, 2020, pp. 546–551.
- [4] Xu, J. W., W. D. Zeng, D. D. Zhou, H. Y. Ma, S. T. He, and W. Chen. Analysis of flow softening during hot deformation of Ti-17 alloy with the lamellar structure. *Journal of Alloys* and Compounds, Vol. 767, 2018, pp. 285–292.
- [5] Balachandran, S., S. Kumar, and D. Banerjee. On recrystallization of the α and β phases in titanium alloys. *Acta Materialia*, Vol. 131, 2017, pp. 423-434.
- [6] Jia, J. B., Y. Yang, Y. Xu, B. Xu, J. T. Luo, and K. F. Zhang. Microstructure evolution and dynamic recrystallization behavior of a powder metallurgy Ti-22Al-25Nb alloy during hot compression. *Materials Characterization*, Vol. 123, 2017, pp. 198-206.
- [7] Quan, G. Z., G. C. Luo, J. T. Liang, D. S. Wu, A. Mao, and Q. Liu. Modelling for the dynamic recrystallization evolution of Ti-6Al-4V alloy in two-phase temperature range and a wide strain rate range. *Computational Materials Science*, Vol. 97, 2015, pp. 136-147.
- [8] Li, J. L., B. Y. Wang, H. Huang, S. Fang, P. Chen, and J. X. Shen. Unified modelling of the flow behavior and softening mechanism of a TC6 titanium alloy during hot deformation. *Journal of Alloys and Compounds*, Vol. 748, 2018, pp. 1031–1043.
- [9] Liu, G. X., D. H. Zhang, and C. F. Yao. A modified constitutive model coupled with microstructure evolution incremental model for machining of titanium alloy Ti-6Al-4V. *Journal of Materials Processing Technology*, Vol. 297, 2021, id. 117262.
- [10] Jiang, Y. Q., Y. C. Lin, G. Q. Wang, G. D. Pang, M. S. Chen, and Z. C. Huang. Microstructure evolution and a unified constitutive model for a Ti-55511 alloy deformed in β region. *Journal of Alloys and Compounds*, Vol. 870, 2021, id. 159534.
- [11] Lin, Y. C., Y. W. Xiao, Y. Q. Jiang, G. D. Pang, H. B. Li, and X. Y. Zhang. K.C. Zhou. Spheroidization and dynamic recrystallization mechanisms of Ti-55511 alloy with bimodal microstructures during hot compression in $\alpha + \beta$ region. *Materials Science & Engineering, A: Structural Materials: Properties, Microstructure and Processing*, Vol. 782, 2020, id. 139282.
- [12] Pang, G. D., Y. C. Lin, Y. L. Qiu, Y. Q. Jiang, Y. W. Xiao, and M. S. Chen. Dislocation density-based model and stacked auto-encoder model for Ti-55511 alloy with basket-weave microstructures deformed in α + β region. Advanced Engineering Materials, Vol. 23, 2021, id. 2001307.
- [13] Cai, Z. W., F. X. Chen, F. J. Ma, and J. Q. Guo. Dynamic recrystallization behavior and hot workability of AZ41M magnesium alloy during hot deformation. *Journal of Alloys and Compounds*, Vol. 670, 2016, pp. 55–63.
- [14] Humphreys, J., G. S. Rohrer, and A. Rollett. *Recrystallization* and related annealing phenomena. 3rd edn. Elsevier, Oxford, 2017. pp. 493–498.

- [15] Liang, H. Q., H. Z. Guo, K. Tan, Y. Q. Ning, X. Luo, G. Cao, et al. Correlation between grain size and flow stress during steady-state dynamic recrystallization. *Materials Science & Engineering, A: Structural Materials: Properties, Microstructure and Processing*, Vol. 638, 2015, pp. 357–362.
- [16] Su, G., Z. Yun, Y. C. Lin, D. G. He, S. Zhang, and Z. J. Chen. Microstructure evolution and a unified constitutive model of Ti-55511 alloy compressed at stepped strain rates. *Materials*, Vol. 14, 2021, id. 6750.
- [17] Lin, Y. C., M. S. Chen, and J. Zhong. Effect of temperature and strain rate on the compressive deformation behavior of 42CrMo steel. *Journal of Materials Processing Technology*, Vol. 205, No. 1–3, 2008, pp. 308–315.
- [18] Seshacharyulu, T., S. C. Medeiros, W. G. Frazier, and Y. V. R. K. Prasad. Hot working of commercial Ti-6Al-4V with an equiaxed $\alpha + \beta$ microstructure: Materials modeling considerations. *Materials Science & Engineering, A: Structural Materials: Properties, Microstructure and Processing*, Vol. 284, No. 1–2, 2000, pp. 184–194.
- [19] Mecking, H. and U. F. Kocks. Kinetics of flow and strain-hardening. Acta Metallurgica, Vol. 29, No. 11, 1981, pp. 1865–1875.
- [20] Jorge Jr, A. M., W. Regone, and O. Balancin. Effect of competing hardening and softening mechanisms on the flow stress curve modeling of ultra-low carbon steel at high temperatures. *Journal of Materials Processing Technology*, Vol. 142, No. 2, 2003, pp. 415–421.
- [21] Raj, S. V. and G. M. Pharr. A compilation and analysis of data for the stress dependence of the subgrain size. *Materials Science and Engineering*, Vol. 81, 1986, pp. 217–237.
- [22] McQueen, H. J. and W. Blum. Dynamic recovery: Sufficient mechanism in the hot deformation of Al (< 99.99). Materials Science & Engineering, A: Structural Materials: Properties, Microstructure and Processing, Vol. 290, No. 1–2, 2000, pp. 95–107.
- [23] Nan, Y., Y. Q. Ning, H. Q. Liang, H. Z. Guo, Z. K. Yao, and M. W. Fu. Work-hardening effect and strain-rate sensitivity behavior during hot deformation of Ti-5Al-5Mo-5V-1Cr-1Fe alloy. *Materials & Design*, Vol. 82, 2015, pp. 84-90.
- [24] Dutta, B., E. Valdes, and C. M. Sellars. Mechanism and kinetics of strain induced precipitation of Nb(C,N) in austenite. Acta Metallurgica et Materialia, Vol. 40, No. 4, 1992, pp. 653–662.
- [25] Jonas, J. J., X. Quelennec, L. Jiang, and É. Martin. The Avrami kinetics of dynamic recrystallization. *Acta Materialia*, Vol. 57, No. 9, 2009, pp. 2748–2756.
- [26] Varshni, Y. P. Temperature dependence of the elastic constants. *Physical Review [Section] B*, Vol. 2, No. 10, 1970, pp. 3952–3958.
- [27] Humphreys, F. J. and M. Hatherly. *Recrystallization and Related Annealing Phenomena*. 2nd edn. Elsevier, Oxford, 2004.
- [28] Favre, J., D. Fabrègue, D. Piot, N. Tang, Y. Koizumi, E. Maire, et al. Modeling grain boundary motion and dynamic recrystallization in pure metals. *Metallurgical and Materials Transactions A: Physical Metallurgy and Materials Science*, Vol. 44, No. 13, 2013, pp. 5861–5875.
- [29] Lin, X. J., H. J. Huang, X. G. Yuan, Y. X. Wang, B. W. Zheng, X. J. Zuo, et al. Study on high-temperature deformation mechanical behavior and dynamic recrystallization kinetics model of Ti-47.5Al-2.5V-1.0Cr-0.2Zr alloy. *Journal of Alloys and Compounds*, Vol. 891, 2022, id. 162105.

- [30] Lin, Y. C., X. M. Chen, D. X. Wen, and M. S. Chen. A physicallybased constitutive model for a typical nickel-based superalloy. Computational Materials Science, Vol. 83, 2014, pp. 282-289.
- [31] Momeni, A., G. R. Ebrahimi, M. Jahazi, and P. Bocher. Microstructure evolution at the onset of discontinuous dynamic recrystallization: A physics-based model of subgrain critical size. Journal of Alloys and Compounds, Vol. 587, 2014, pp. 199-210.
- [32] Chen, X. M., Y. C. Lin, D. X. Wen, J. L. Zhang, and M. He. Dynamic recrystallization behavior of a typical nickel-based superalloy during hot deformation. Materials & Design, Vol. 57, 2014, pp. 568-577.
- [33] Sha, W. and S. Malinov. Titanium Alloys: Modelling of Microstructure, Properties and Applications, Woodhead Publishing, Cambridge, 2009.
- [34] Wang, M. H., Y. F. Li, W. H. Wang, J. Zhou, and A. Chiba. Quantitative analysis of work hardening and dynamic softening behavior of low carbon alloy steel based on the flow stress. Materials & Design, Vol. 45, 2013, pp. 384-392.

- [35] Quan, G. Z., D. S. Wu, G. C. Luo, Y. F. Xia, J. Zhou, Q. Liu, et al. Dynamic recrystallization kinetics in α phase of as-cast Ti-6Al-2Zr-1Mo-1V alloy during compression at different temperatures and strain rates. Materials Science & Engineering, A: Structural Materials: Properties, Microstructure and Processing, Vol. 589, 2014, pp. 23-33.
- [36] Liang, H. Q., H. Z. Guo, Y. Q. Ning, X. N. Peng, C. Qin, Z. F. Shi, et al. Dynamic recrystallization behavior of Ti-5Al-5Mo-5V-1Cr-1Fe alloy. Materials & Design, Vol. 63, 2014, pp. 798-804.
- [37] Wang, J., K. L. Wang, S. Q. Lu, X. Li, D. L. OuYang, and Q. Qiu. Softening mechanism and process parameters optimization of Ti-4.2Al-0.005B titanium alloy during hot deformation. Journal of Materials Research and Technology, Vol. 17, 2022, pp. 1842-1851.
- [38] Xu, J. W., W. D. Zeng, X. Y. Zhang, and D. D. Zhou. Analysis of globularization modeling and mechanisms of alpha/beta titanium alloy. Journal of Alloys and Compounds, Vol. 788, 2019, pp. 110-117.